Two-point concrete resistivity measurements

Two-point concrete resistivity measurements: interfacial phenomena at the electrode-concrete contact zone

.

W. J. McCarter [#], H. M. Taha, B. Suryanto, G. Starrs

Heriot Watt University,

School of Energy, Geoscience, Infrastructure and Society,

Institute for Infrastructure and Environment,

Edinburgh, EH14 4AS, Scotland,

U.K.

Corresponding Author:

E-mail: **w.j.mccarter@hw.ac.uk**

Tel: +44-131-451-3318
Fax: +44-131-451-4617

ABSTRACT

A.C impedance spectroscopy measurements are used to critically examine the *end-to-end* (two-point) testing technique employed in evaluating the bulk electrical resistivity of concrete. In particular, this paper focusses on the interfacial contact region between the electrode and specimen and the influence of contacting medium and measurement frequency on the impedance response. Two-point and four-point electrode configurations were compared and modelling of the impedance response was undertaken to identify and quantify the contribution of the electrode-specimen contact region on the measured impedance. Measurements are presented in both Bode and Nyquist formats to aid interpretation. Concretes mixes conforming to BSEN206-1 and BS8500-1 were investigated which included concretes containing the supplementary cementitious materials fly-ash and ground granulated blast-furnace slag. A measurement protocol is presented for the *end-to-end* technique in terms of test frequency and electrode-specimen contacting medium in order to minimise electrode-specimen interfacial effect and ensure correct measurement of bulk resistivity.

Keywords: concrete; supplementary cementitious materials; a.c. impedance; two-point electrode; four-point electrode

1.0 INTRODUCTION

The addition of water to Portland cement clinker produces a series of complex hydrolysis and hydration reactions causing a transformation of the viscous suspension of cement particles to a porous solid. The microporous nature of hardened cement has a significant influence its permeation properties and, consequently, has implications in the durability and performance of cement-based materials such as concrete. One of the most serious (world-wide) problems associated with reinforced concrete structures is corrosion of the reinforcing steel due to the ingress of chloride ions – either from the marine environment or from deicing salt used on roads for winter maintenance purposes. In the design of durable concrete structures, there exists a need to determine those characteristics of concrete which promote the ingress of gases and/or liquids containing dissolved contaminants and defining the performance of a concrete in terms of an easily measured parameter. Regarding the durability of concrete, strength, per se, is not a requirement, and properties such as absorption, diffusion and permeability are more important in this respect [1]. The permeation properties of concrete will be intimately linked to the capillary pore network within the cementitious matrix which, in turn, will be influenced by the cement-content, water-content and the addition of admixtures and supplementary cementitious materials (SCM) such as fly ash and ground granulated blast-furnace slag.

As the flow of water under a pressure gradient (hence permeability) or the movement of ions under a concentration gradient (hence diffusivity) is analogous to the conduction of electrical current under a potential gradient, the electrical properties of concrete (viz. resistivity or, its reciprocal, conductivity) are being increasingly considered as a 'durability index' for assessing the long-term performance of concrete structures [see, for example 2-10]. Furthermore, as capillary pore tortuosity, pore connectivity and pore constriction all influence

the electrical properties of concrete, an electrical property measurement could thus quantify those microstructural characteristics which are of importance in assessing the durability of concrete structures. Table 1 [6] and Table 2 [11, 12] present a concrete durability classification system based on electrical resistivity measurements.

In the development of standardised procedures for the measurement of the electrical properties of concrete - resistivity/conductivity in this instance - an a.c. *end-to-end*, or two-electrode test method, is normally used with contact between the concrete specimen and electrodes via water saturated sponges [2, 13]. In terms of the a.c. test frequency, no particular value is specified, although a frequency in the range 50-100Hz has been recommended [13, 14]. In the measurement of concrete resistivity using two- and four-electrode methods, a frequency in the range 50Hz-1kHz has also been suggested [15]. More specifically, frequency values of 108Hz [2], 128 Hz [16] and 107Hz and 120Hz [17] have been used for two-electrode measurements.

As electrical property measurements – bulk resistivity in this instance - could, ultimately, be developed and exploited as an important concrete durability indicator, evaluation of this parameter is of considerable importance. This paper critically examines the end-to-end technique used for bulk resistivity measurements. Of particular interest in the current work is the influence of the electrode-specimen contact region on the measured electrical impedance and, to this end, electrical impedance spectroscopy is used with measurements taken over the frequency range 1Hz-10MHz.

2.0 EXPERIMENTAL PROGRAMME

2.1 Materials and Sample Preparation

The concrete mixes used within the experimental programme are presented in Table 3. The cementitious binders[♦] comprised Portland cement (PC) clinker, CEM I 52.5N to EN197-1 [18]; CEM I cement blended with ground granulated blast-furnace slag (GGBS) to EN15167-1 [19]; and CEM I cement blended with low-lime fly-ash (FA) to EN450-1 [20]. An oxide analysis of these materials is presented in Table 4. Crushed granite aggregate, both coarse and fine, was used throughout together with a mid-range water reducer/plasticiser (SikaPlast 15RM) conforming to EN934-2 [21]. The PC and SCM's were combined at the concrete pan-mixer. Regarding reinforced concrete structures, the range of mixes presented in Table 3, in terms of binder-content, binder composition, water-binder (w/b) ratio and grade strength satisfy (or exceed) the minimum requirements specified in Eurocode EN206-1:2000 [22] and British Standard BS8500-1 [23] for environmental exposure classes XC (corrosion induced by carbonation), XS (corrosion induced by chlorides from sea-water) and XD (corrosion induced by chlorides other than sea-water e.g. deicing salt) for an intended working life of 100 years, with a minimum of 0.05m cover-to-steel.

Samples were cast as 0.15×0.15×0.15m cube specimens in steel moulds and a total of three were cast for each mix on Table 3; six, 0.10×0.10×0.10m cubes were also cast, for compressive strength tests at 28-days and 180-days and are presented in Table 3, denoted, respectively, F_{28} and F_{180}. Specimen sizes conformed to EN12390-1 [24] and made in accordance with EN12390-2 [25] and were thus considered sufficiently large to ensure that local inhomogeneities would not have any appreciable influence on the bulk impedance response; compressive strength testing was carried out in accordance with EN12390-3 [26].

♦ The binder comprises the total cementitious content of the concrete mix i.e. PC and SCM.

Stainless steel pin-electrodes were positioned centrally within each sample at the time of casting which ensured intimate contact between the electrodes and the surrounding concrete. Each electrode comprised a 0.0023m diameter stainless-steel (s/s) rod (approximately 0.10m in length); the rod was sleeved with heat-shrink insulation to expose a 0.01m length of tip with the centre-to-centre spacing between the electrodes being 0.075m. These electrodes were used for four-point electrical measurements and discussed below. A thermistor was attached to one of the electrodes to allow the cube temperature to be recorded. Samples were stored in a curing tank (21°C±2°C) until required for testing which, for the current work programme, was at approximately 36 months. At this age, the change in resistivity/conductivity due to hydration will be negligible [27]; furthermore, it is only at such longer time-scales that the influence of the FA and GGBS on pore-structure becomes evident.

2.2 Electrical Measurements and Data Acquisition

Two-point electrical impedance measurements were obtained on each sample using a Solartron 1260 frequency response analyser (FRA). The signal amplitude used in the experimental programme was 350mV with the impedance measured over the frequency range 1Hz-10MHz using a logarithmic sweep with 10 frequency points per decade. The measured impedance comprised both the in-phase (resistive) component and quadrature (reactive) component. After removal from the curing tank, the concrete cube was wiped with an absorbent towel and allowed to surface-dry before testing (to negate any possible surface conduction effects) with testing undertaken in a laboratory at a temperature of 21°C±1°C.

Fig. 1(a) presents a schematic of the two-electrode testing arrangement. In this Figure, external stainless steel (s/s) plate-electrodes were placed against opposite faces of the concrete cube (i.e. the faces cast against the steel mould). Intimate contact between the electrodes and concrete was obtained by means of 0.15×0.15m synthetic sponges, each

0.002m thick, saturated with a contact solution. Leads from the current (I_{output}) and potential (V_{high}) connections on the FRA were coupled at one of the electrodes and the current (I_{input}) and potential (V_{low}) connections coupled at the other electrode. Open- and short- circuit residual lead impedances were automatically *nulled* from the measurements at every spot frequency using the FRA's on-board lead-correction facility. The overall testing arrangement is displayed in Fig. 1(b) with a mass of 2kg placed on the upper electrode to ensure uniform contact and giving a contact pressure of approximately 1kPa. Regarding the contact solution noted above, three were used in the current experimental program with separate sets of sponges were used for each saturating liquid:

(a) mains tap-water;

(b) a saturated solution of calcium hydroxide [28] (as calcium hydroxide is released during the hydration of the silicate phases within the cement clinker); and,

(c) a simulated cement pore-solution comprising 0.1 molar sodium hydroxide and 0.3 molar potassium hydroxide [29, 30] (as the alkali-oxides - Na_2O and K_2O - within the cement clinker are highly soluble).

The impedance response of the sponges placed between the electrodes, loaded as above, was measured separately at the end of each test. In addition to two-electrode measurements, a four-electrode testing configuration was also used and shown schematically in Fig. 2(a). In this set-up, the external s/s plate-electrodes served as the current (output/input) electrodes and the embedded s/s rods acted as the potential (high/low) electrodes. Fig. 2(b) displays the testing arrangement with the plates placed on the faces perpendicular to the embedded pin-electrodes. In this Figure, the spacing s = 0.075m.

In connection with bulk resistivity measurements on concrete, it is generally accepted that electrodes should be spaced apart at least 1.5 times the maximum aggregate size [31] to obtain values representative of the bulk material. The maximum aggregate size used in the

experimental programme was 20mm, hence electrode spacings should be >30mm which is the case for both the external plate-electrodes and internal pin-electrodes.

3.0 TEST RESULTS AND DISCUSSION

3.1 Two-Electrode Measurements

Preliminaries

It has been shown that the impedance of a cementitious material, $Z^*(\omega)$ (in ohms, Ω), can be represented in complex format through the relationship [32],

$$Z^*(\omega) = Z'(\omega) - iZ''(\omega) \qquad (1)$$

where ω is the angular frequency (= $2\pi f$ and f is the frequency of the applied field in Hz), $Z'(\omega)$ is the real or resistive component, $Z''(\omega)$ is the imaginary or reactive component and $i = \sqrt{-1}$. Two presentation formalisms are used:

(i) Nyquist format i.e. $-iZ''(\omega)$ *vs* $Z'(\omega)$, which is the polar plot.

(ii) Bode format. This plot highlights the frequency domain behaviour of both the impedance, $|Z^*(\omega)|$, and phase angle, θ ($= tan^{-1}\left(\frac{Z''(\omega)}{Z'(\omega)}\right)$. A phase angle θ = -90° would represent purely capacitive behaviour whereas a phase angle θ = 0° would represent purely resistive behaviour.

Regarding the Nyquist formalism in (i) above, if the system can be electrically modelled as a resistor in parallel with a pure capacitor whose capacitance (in Farads) is constant with increasing frequency, the polar plot will take the form of a semi-circle. Fig. 3(a) displays the plot for a resistor/capacitor combination with R=1.0 kΩ and C=10^{-10} F, which produces a semi-circle whose centre is located on the real axis. Frequency increases from right to left across the plot. However, for porous media such as cementitious materials (see, for example,

references 32-36), the plot takes the form of a circular arc whose centre is depressed below the real ($Z'(\omega)$) axis. This is due to relaxation of polarization processes within the system and results in dielectric dispersion i.e. the decrease in the capacitance with increasing frequency. To account for this phenomenon, the capacitive reactance is replaced by a pseudo capacitance or constant phase element (CPE) to account for the dispersive behaviour of the medium. The CPE is a complex, frequency-dependent parameter defined by the relationship,

$$Z''_{CPE}(\omega) = \frac{1}{C_o(i\omega)^p} \qquad (2)$$

where $i = \sqrt{-1}$, C_o is a coefficient and the exponent, p, has a value such that $0<p<1$; if p equals 1, then the equation is identical to the reactive component of a pure capacitor of value C_o with units in farads (F). When a CPE with value of $p<1$ is placed in parallel with a resistor, a circular arc is produced with its centre depressed below the real axis with C_o having units $Fs^{(p-1)}$. Fig. 3(a) also presents the Nyquist plot for a CPE ($C_o = 10^{-10}$ $Fs^{-0.2}$ and p=0.8) in parallel with a resistor R=1.0kΩ which now results a circular arc with its centre below the real axis. With reference to the schematic diagram in Fig. 3(b), the depression angle, α (in degrees) of the circle centre (O), is related to the exponent, p, in equation (2) through the relationship,

$$\alpha = 90^o(1-p) \qquad (3)$$

General Observations and Impedance Modelling

Fig. 4 presents the Nyquist plots with only the sponges placed between the electrodes, saturated with the three different liquids: water, calcium hydroxide and simulated pore-solution. This Figure indicates an almost linear decrease with increasing frequency and would represent part of a much larger arc associated with polarization phenomena at the electrode-sponge interface; the full extent of this arc would only become evident at frequencies

considerably lower than the current work, i.e. <1Hz. Regarding Fig. 4, the plots converge on the real axis as the frequency increases and, in all cases, at a frequency of approximately 40kHz touches the real axis; this point gives the bulk resistance of the sponges. Some residual lead inductive effects are evident in this Figure as the reactance turns positive at frequencies in excess of 40kHz. Regarding the sponge resistance at 40kHz, these value are, 7.9Ω, 2.8Ω and 0.75Ω for, respectively, the sponges saturated with water, calcium hydroxide and simulated pore-solution.

Figs. 5-7 display the impedance response for the concrete mixes in Table 3 using the testing arrangement presented in Fig. 1(a), with the simulated pore-solution used as the sponge saturating liquid. Note, that for reasons of clarity, only every third data marker has been highlighted on these plots although the curves have been drawn through all data points. The Nyquist plots in these Figures represent the mean value for the three notionally identical specimens with salient frequencies indicated. On the Bode plots, error bars have been included to highlight the frequency-dependent variation in measurements between the replicate specimens, with the error bars representing ±one standard deviation. Where error bars appear to be absent, the data markers are larger than the error bars. A feature evident from the Bode plots indicates that the scatter in the measurements from notionally identical specimens reduces with increasing frequency.

Generally, each response has a single dominant circular arc (denoted arc-1) similar to the schematic shown in Fig. 3(b); however, the frequency range over which this arc dominates, the frequency at which it maximizes, the arc diameter and depression angle (α) are all dependent on the concrete mix proportions. On closer examination, a second small, flat arc (denoted arc-2) is evident at the at the low-frequency end of the Nyquist plots (right-hand-side) presented in Figs. 5-7. In some instances, a small *spur* is also present of the right-hand-

side of the plot -see, for example, Fig. 5(a). In terms of representing the response as an electrical circuit, this is presented in Fig. 8 and comprises four, series-connected, parallel circuit elements (the bulk resistance of the sponges has been omitted from this model as their resistance is negligible in comparison to the impedance of the system):

(i) a resistor R_s which represents the projected intercept of the high-frequency end of the arc-1 with the real axis. This would assume that there is finite resistance at infinite frequency which is clearly not tenable and would imply that a further high frequency arc exists i.e. there would be a constant-phase element (CPE) in parallel with R_s as the plot must eventually go through the origin. However, as the upper limit of the current investigation was 10MHz and no data were recorded at frequencies >10MHz, the circuit has simply been left as a single, shunted, resistive element;

(ii) a parallel combination of resistor, R, and constant-phase element, CPE, for both arc-1 (R1 and CPE1) and arc-2 (R2 and CPE2);

(iii) the small spur at the low-frequency end of the response would represent part of a much larger arc which would only become evident at frequencies <1Hz. For completeness, this is also represented by a parallel combination of resistor (R3) and constant phase element (CPE3) although is not present in some of the concrete mixes.

In attempting to offer a phenomenological interpretation for the circuit, consider again the testing arrangement in Fig. 1(a). There are two interfaces present in this arrangement: the electrode-sponge interface and the sponge-concrete interface. If each interface can be electrically modelled as a parallel combination of resistor and CPE, then R3-CPE3 (exponent P3) would account for the response from the electrode-sponge interface; R2-CPE2 (exponent P2) the response from the sponge-specimen interface, and R1-CPE1 (exponent P1) and R_s the *bulk* response from the concrete specimen. Consider, for example, the Nyquist plots for the

PC mix (w/b=0.65) and the GGBS mix (w/b=0.35) presented in Figs. 5 and 6 respectively; using the parameter values for the circuit elements presented in Table 5, the simulated Nyquist responses (in ZView, Scribner Associates, Inc.) over the frequency range 1Hz-10MHz are presented in Figs. 9(a) and (b). For reasons of clarity, data markers have been removed from both the measured and simulated plots. The simulated circuit and the measured data show good agreement indicating that the model is a good electrical representation of the system. Regarding the GGBS concrete (Fig 9(b)), as this mix did not display a *spur* in the low-frequency region circuit element R3-CPE3 is not included in the model simulation.

The following general features are evident from Figs. 5-7:

(a) an increase in the w/b ratio results in a decrease in the bulk impedance of the specimen causing a decrease in the diameter of the dominant (bulk) arc (i.e. circuit element R1-CPE1). R1, together with R_s, would represent the resistance associated with the continuous capillary porosity within the concrete i.e. the percolated porosity;

(b) concretes containing SCM's have an increased impedance in comparison to the equivalent PC mix. Although concretes containing GGBS and fly-ash may not necessarily be of lower total porosity than the PC concretes, it is of a much more disconnected and tortuous nature [37, 38]. This feature is reflected in the increased impedance of these mixes.

(c) the frequency at which the R1-CPE1 arc maximizes falls within the range 150kHz-5MHz and is binder-specific with the maximum frequency increasing in the order FA concretes, GGBS concretes followed by PC concretes; and,

(d) the exponent, *p*, for the circuit element CPE1 falls within a relatively narrow range for each concrete and is binder specific: 0.92-0.96 for the PC concretes; 0.80-0.82 for the

GGBS concretes, and, 0.74-0.75 for the FA concretes. From equation (3) above, this implies that the arc depression angle, α, for the R1-CPE1 circuit element increases as the impedance of the concrete increases.

Sponge saturating liquid

In order to confirm if circuit elements R2-CPE2 and R3-CPE3 are, indeed, artefacts of the concrete/electrode contacting medium, Figs. 10-12 present the Nyquist and Bode plots for the concrete mixes (w/b = 0.65 only) with the contacting sponges saturated with tap water, calcium hydroxide and simulated pore solution. These figures clearly highlight the influence of the saturating liquid on the impedance response. As previously noted, for sponges saturated with the simulated pore solution, this manifests itself as a small, flat arc at the low frequency side of the Nyquist plot, but as the impedance of the sponges increases (see Fig. 4), it can be seen that this flat arc develops into a well-defined, low frequency circular arc. The Bode plots show more clearly the influence of the sponge saturating liquid on the measured impedance, $|Z^*(\omega)|$, and phase angle, θ, as the impedance curves, and phase angle curves, tend to merge in the frequency range 5kHz-10kHz. At frequencies in excess of approximately 5kHz, the circuit model for the system would then be represented by R1-CPE1 and R_s in Fig. 8. It is also evident that as the impedance of the concrete specimen increases, the influence of the sponge saturating liquid diminishes.

This clearly has implications in the development of standard testing procedures for concrete resistivity measurements, particularly using a.c. in the low-frequency range 50-100Hz. For example, consider the PC (w/b=0.65) concrete in Fig. 10; using water-saturated sponges, the measured resistance (real component), R, at 100Hz is 804Ω, whereas at 10kHz the resistance is 593 Ω. The resistance of the sponges measured separately, denoted R_{sp}, is 9.4 ohms at 100Hz and 8.1 ohms at 10kHz. Using the method presented in references [13] and [16], these

values could then be used to evaluate the bulk resistivity of the concrete cube (ρ_{cube}) using the two-point method presented in Fig. 1(a) as,

$$\rho_{cube} = \frac{A}{L}\left(R - R_{sp}\right) \qquad (4)$$

where A is the cross-sectional area through which the current flows (0.15m×0.15m) and L is the spacing between the electrode plates (0.15m). This obtains a resistivity of 119Ωm at 100Hz and 88Ωm at 10kHz. With reference to Table 2, this would move the concrete from one classification into another based solely on the test frequency and sponge saturating liquid. Both these parameters need to be standardised to provide a consistent measurement procedure/protocol. This leaves the question, how is the true bulk resistance (hence resistivity/conductivity) of the specimen obtained using a two-point (end-to-end) measurement technique? This is further explored in the next section.

Four-Electrode Measurements

The model presented in Fig. 8(a) would suggest that the bulk resistance of the concrete can be obtained at the intercept of the low-frequency end of arc R1-CPE1 with the real axis (i.e. the value R_s +R1). In the two-electrode technique, the potential drop is measured between the external plate electrodes which includes the spurious effects the sponges have on the measured impedance. By separating the current electrodes and potential electrodes as presented in Fig. 2(a), such effects are, theoretically, eliminated. Ideally, in the four–electrode method the potential electrodes should be moved out of the current field to ensure that no current is drawn to the sensing electrodes [39, 40]. It was decided, however, to use embedded voltage-sensing pin-electrodes as the FRA's input impedance - 1.0Mohm over the frequency range 1Hz-10kHz then decreasing to 45kohm at 10MHz [41] - is considerably

larger than the impedance being measured which will ensure that negligible current is drawn through the sensing electrodes.

As way of illustration, using the testing arrangement in Fig. 2(a), Fig. 13(a) presents the Bode plots for the PC concrete (w/b=0.65) and Fig. 13(b) that for the GGBS concrete (w/b=0.35) with simulated pore solution used to saturate the contact-sponges (as before, for clarity, only every third data point has been highlighted). With the electrode/sponge effect absent, the elements R2-CPE2 and R3-CPE3 (see Fig. 8(a)) are, effectively, removed and the impedance and phase angle remain virtually constant over the frequency range 1Hz-10kHz. As the phase angle is ~0°, this implies that the concrete is displaying purely resistive behaviour and $Z^*(\omega) \approx Z'(\omega)$. Consider now the resistance of the concrete specimens at 1kHz (which lies near the logarithmic centre of this frequency range); from Fig. 13, this obtains values of 272Ω for the PC mix and 2219 Ω for the GGBS mix. As the current flow-lines through the sample are parallel, the resistivity of the concrete, ρ_{conc} (in ohm-m), can be evaluated,

$$\rho_{conc} = \frac{A}{d} R \qquad (5)$$

where R is the measured resistance (real component) for this testing configuration, d is the spacing of the embedded potential electrodes (0.075m) and A is the cross-sectional area through which the current flows (0.15m×0.15m). This gives a resistivity for the concretes of 81.6Ωm for the PC mix and 666Ωm for the GGBS mix. These values can now be used to compute the bulk resistance of the concrete cube (R_{cube}) using the two-point method,

$$R_{cube} = \frac{L}{A} \rho_{conc} \qquad (6)$$

where A is defined above and L is the spacing between the electrode plates (0.15m); hence R_{cube} = 544Ω for the PC mix and 4440Ω for the GGBS. These represent the real component of the impedance, $Z'(\omega)$, which are now located on the Nyquist plots presented in Fig. 5(a) and Fig. 6(a) and indicated by an arrow on the real axis. This procedure was repeated for all the concrete mixes in Table 3 and indicated accordingly on the Nyquist plot associated with each mix in Figs. 5-7. It is apparent that the true resistance of the cube can generally be located at the cusp-point between the sponge/specimen interface arc (R2-CPE2 on Fig. 8(a)) and the bulk concrete arc (R1-CPE1 on Fig. 8(a)).

In terms of standardizing testing procedures using a single frequency, end-to-end (two-point) resistance measurement, the work detailed above would indicate that the test frequency should lie in the range 5kHz-10kHz together with a highly conductive sponge saturating liquid.

4. CONCLUSION AND CONCLUDING COMMENTS

Impedance spectroscopy was used to obtain the electrical properties of concrete over the frequency range 1Hz-10MHz. Concretes used in the test programme comprised PC concretes and concretes containing either GGBS or FA as a partial replacement. Measurements were presented in both Nyquist and Bode formats which gave a detailed picture of the electrical response of the electrode-concrete system with synthetic sponges used to form an electrical contacting medium between the electrode and concrete specimen. The following general conclusions can be drawn,

(i) An equivalent electrical model for the system was presented which comprised series connected parallel circuit elements to represent the concrete specimen, the sponge/specimen interface and the sponge/electrode interface. The parallel circuit

elements consisted of a resistor, R, and constant phase element (CPE), with the CPE being introduced to take account of the dispersion in capacitance with frequency.

(ii) It was observed that using saturated sponges as an electrode/specimen contacting medium introduced a spurious circuit element represented by the sponge/specimen interface. Additionally, the sponge saturating liquid had a significant influence on the impedance response of the electrode-sponge-specimen system; as the impedance of the saturating liquid increased a well-defined, low-frequency arc developed in the Nyquist plot. However, as the frequency of the applied field increased, the influence of the electrode/sponge and sponge/specimen interfaces decreased.

(iii) The electrical impedance of the concrete mixes was strongly related to the w/b ratio and the type of cementitious binder. Increasing the w/b ratio resulted in a decrease in the overall impedance of the system whereas the addition of GGBS and FA increased the impedance of the system. Additionally, using the Nyquist formalism, several interdependent parameters of the arc associated with the bulk concrete response (circuit element R1-CPE1) were identified - the arc depression angle, α, and the frequency at which the arc R1-CPE1 maximized; both these parameters tended to be more influenced by binder-type and less by w/b ratio.

(iv) Four-point impedance measurements were presented which indicated that the specimens displayed purely resistive behaviour (phase angle $\approx 0°$) over the frequency range 1Hz-10kHz. These measurements allowed evaluation of the bulk resistivity of the concrete. The resistance (real component) of the cube calculated from 4-point resistivity measurements was located on the Nyquist plot and occurred at the low-frequency side of the circuit element representing the bulk response (R1-CPE1).

Regarding the testing procedure for two-point, end-to-end resistivity measurements, the work presented would suggest that using an a.c. frequency in the range 5kHz-10kHz with a low resistivity liquid used to saturate the sponges would result in a more accurate assessment in concrete resistivity/conductivity. This is particularly important for low resistivity concrete mixes bearing in mind that the experimental programme was undertaken on mature concrete samples as hydration and the pozzolanic reaction would be negligible and measurements would reflect the differences in the fully developed pore structure. During the early stages of hydration, young concretes would display considerably lower impedance values and hence sponge contacting medium would have a much greater influence on the two-point measurement with consequent greater error if a standard procedure is not developed.

Acknowledgments

One of the Authors (HMT) wishes to acknowledge the financial support provided by Heriot Watt University.

Table 1: Suggested ranges for concrete durability classification (adapted from [6]). Note: in this test, specimens are vacuum saturated with 5.0M NaCl solution prior to the measurement.

Durability class	Chloride Resistivity Index (ohm-m)
Excellent	>13.0
Good	6.50-13.0
Poor	4.00-6.50
Very poor	<4.00

Table 2: Empirical concrete resistivity thresholds for protection of embedded steel reinforcement (adapted from [11, 12]).

Resistance to corrosion	Resistivity (ohm-m)
Low	< 50
Moderate / Low	50 - 100
High	100 - 200
Very High	> 200

Table 3: Summary of concrete mixes (w/b = water/(cement+SCM) ratio; Pl = plasticiser).

Mix Designation	w/b	CEM I kg/m^3	GGBS kg/m^3	FA kg/m^3	20mm kg/m^3	10mm kg/m^3	Fine (<4mm) kg/m^3	Pl l/m^3	F_{28} MPa	F_{180} MPa
PC	0.35	378	-	-	787	393	787	5.15	79	88
	0.65	263	-	-	790	395	790	-	39	46
GGBS	0.35	245	132	-	784	392	784	5.13	81	89
	0.65	171	92	-	788	394	788	-	35	45
FA	0.35	242	-	130	773	386	773	5.06	65	81
	0.65	169	-	91	780	390	780	-	24	38

Table 4: Oxide analysis of cementitious materials (+ = not determined)

% by weight	PC	FA	GGBS
SiO_2	20.68	51.0	34.33
Al_2O_3	4.83	27.4	12.60
Fe_2O_3	3.17	4.6	0.60
CaO	63.95	3.4	41.64
MgO	2.53	1.4	8.31
TiO_2	+	1.6	+
P_2O_5	+	0.3	+
SO_3	2.80	0.7	+
K_2O	0.54	1.0	0.47
Na_2O	0.08	0.2	0.25

Table 5: Circuit simulation parameters for PC and GGBS concrete mixes (+ = not determined).

Mix	R_s ohm	R1 ohm	CPE1 (C_o) $Fs^{(P1-1)}$	P1	R2 ohm	CPE2 (C_o) $Fs^{(P2-1)}$	P2	R3 ohm	CPE3 (C_o) $Fs^{(P3-1)}$	P3
PC (w/b=0.65)	129	348	1.929×10^{-10}	0.96	114	1.160×10^{-4}	0.314	5×10^{5}	3.77×10^{-3}	0.768
GGBS (w/b=0.35)	44.9	4148	1.072×10^{-9}	0.80	1333	2.729×10^{-5}	0.429	+	+	+

References

[1] Basheer PAM, Barbhuiya S. Pore structure and transport processes. Chapter 2 in Concrete durability: A practical guide to the design of durable concrete structures (M Soutsos, Editor) Thomas Telford Ltd., London, 2010 (ISBN 978-0-7277-3517-1)

[2] Gehlen C, Ludwig H-M. Compliance testing for probabilistic design purposes. DuraCrete EU-Brite EuRam III 1999; March; ISBN 903760420X

[3] Torrents JM, Juan-García P, Aguado A. Electrical impedance spectroscopy as a technique for the surveillance of civil engineering structures: considerations on the galvanic insulation of samples. *Meas. Sci. Technol.*, 2007;18; 1958–62

[4] Alexander MG, Ballim Y, Stanish KA. Framework for use of durability indexes in performance-based design and specifications for reinforced concrete structures. *Mater. Struct.*, 2008; 41(5); 921-36

[5] Andrade C. Types of Models of Service Life of Reinforcement: The Case of the Resistivity. *Concrete Research Letters*, 2010; 1(2); June; 73-80

[6] Alexander MG, Santhanam M, Ballim Y. Durability design and specification for concrete structures - the way forward. *Int. J. Adv. Eng. Sci. Appl. Math*., 2010; 2(3); 95-105

[7] Muigai R, Moyo P, Alexander M. Durability design of reinforced concrete structures: a comparison of the use of durability indexes in the deemed-to-satisfy approach and the full-probabilistic approach. *Mater. Struct.*, 2012; 45(8); 1233-44

[8] Andrade C, Prieto M, Tanner P, Tavares F, d'Andrea R. Testing and modelling chloride penetration into concrete. *Construction and Building Mater.*, 2013; 39(February); 9-18

[9] Nganga G, Alexander M, Beushausen H. Practical implementation of the durability index performance-based design approach. *Construction and Building Mater.,* 2013; 45(August); 251-61

[10] Andrade C, d'Andrea R, Rebolledo N. Chloride ion penetration in concrete: The reaction factor in the electrical resistivity model. *Cement Concrete Comp.,* 2014; 47(March); 41-6

[11] Langford P, Broomfield JP. Monitoring the corrosion of reinforcing steel *Construction and Repair,* 1987; May; 32-6

[12] Broomfield JP. Corrosion of steel in concrete. 1st ed. E&FN Spon, London, 1997 (ISBN 0 419 19630 7)

[13] Luping T. Resistance of concrete to chloride ingress – from laboratory tests to in-field performance. EU-Project (5th FP GROWTH) G6RD-CT-2002-00855; 2005; Deliverable D22 Testing Resistance of Concrete to Chloride Ingress – A proposal to CEN for consideration as EN standard. Available at: http://www.civil.ist.utl.pt/~cristina/RREst/Aulas_Apresentacoes/07_Bibliografia/durabilidade%20betao%20%28durability%29/Outros/Guidline%20different%20method%20choloride%20ingress.pdf (accessed 4th May 2015)

[14] Spanish Association for Standardization and Certification. Durability of concrete: Test methods: Determination of the electrical resistivity. Part 1: Direct method (reference method) PNE 83988-1: 2008

[15] Polder R. Electrochemical techniques for measuring metallic corrosion. *Mater. Struct.,* 2000; 33(10); 603-11

[16] Newlands M D, Jones M R, Kandasami S, Harrison TA. Sensitivity of electrode contact solutions and contact pressure in assessing electrical resistivity of concrete. *Mater. Struct.,* 2008; 41(4); 621-32

[17] Osterminski K, Polder RB, Schiessl P. Long term behaviour of the resistivity of concrete. *HERON,* 2012; 57(3); 211-30

[18] British Standards Institution. Cement-Part 1: Composition, specifications and conformity criteria for common cements, BSI, London, EN197-1:2000

[19] British Standards Institution. Ground granulated blast furnace slag for use in concrete, mortar and grout - Part 1: Definitions, specifications and conformity criteria. BSI, London, EN15167-1:2006

[20] British Standards Institution. Fly ash for concrete-Part 1: Definition, specifications and conformity criteria. BSI, London, EN450-1:2005

[21] British Standards Institution. Admixtures for concrete, mortar and grout. Part 2: Concrete admixtures. BSI, London, EN934-2:2009

[22] British Standards Institution. Concrete: Specification, performance, production and conformity. BSI, London, EN206-1:2000

[23] British Standards Institution. Concrete - Complementary British Standard to EN 206-1-Part 1: Method of specifying and guidance for the specifer. BSI, London, BS8500-1:2006

[24] British Standards Institution. Testing hardened concrete Part 1: Shape, dimensions and other requirements for specimens and moulds. BSI, London, EN12390-1:2012

[25] British Standards Institution. Testing hardened concrete Part 2: Making and curing specimens for strength tests. BSI, London, EN12390-2:2009

[26] British Standards Institution. Testing hardened concrete Part 3: Compressive strength of test specimens. BSI, London, EN12390-3:2009

[27] Whittington HW, McCarter J, Forde MC. The conduction of electricity through concrete. *Mag. Concrete Res.*, 1981; 33(114); 48-60

[28] Saremi M, Mahallati E. A study on chloride-induced depassivation of mild steel in simulated concrete pore solution. *Cement Concrete Res.*, 2002; 32(12); 1915-21

[29] Ghods P, Isgor OB, Carpenter GJC, Li J, McRae GA, Gu GP. Nano-scale study of passive films and chloride-induced depassivation of carbon steel rebar in simulated concrete pore solutions using FIB/TEM. *Cement Concrete Res.*, 2013; 47(May); 55-68

[30] Yang Z, Fischer H, Polder R. Synthesis and characterization of modified hydrotalcites and their ion exchange characteristics in chloride-rich simulated concrete pore solution. *Cement Concrete Comp*., 2014; 47(March); 87-93

[31] du Plooy R, Palma-Lopes S, Villain G, Dérobert X. Development of a multi-ring resistivity cell and multi-electrode resistivity probe for investigation of cover concrete condition. *NDT&E International*, 2013; 54(March); 27–36

[32] McCarter WJ, Brousseau R. The A.C. response of hardened cement paste. *Cement Concrete Res.*, 1990; 20(6); 891-900

[33] Christensen BJ, Coverdale RT, Olsen RA, Ford SJ, Garboczi EJ, Jennings HM, Mason TO. Impedance Spectroscopy of Hydrating Cement-based Materials: Measurement, Interpretation, and Applications. *J. Am. Ceram. Soc.*, 1994; **77**(1); 2789–2804

[34] Keddam M, Takenouti H, Novoa X R, Andrade C, Alonso C. Impedance Measurements on Cement Paste. *Cement Concrete. Res*., 1997; 27(8); 1191–1201

[35] Cabeza M, Merino P, Miranda A, Nóvoa XR, Sanchez I. Impedance Spectroscopy Study of Hardened Portland Cement Paste. *Cement Concrete. Res.*, 2002; 32(6); 881–891

[36] Ball RJ, Allen GC, Starrs G, McCarter WJ. Impedance spectroscopy measurements to study physio-chemical processes in lime-based composites. *Applied Physics A: Materials Science & Processing*, 2011; 105 (3); Nov; 739-751

[37] Li S, Roy DM. Investigation of relations between porosity, pore structure, and $C1^-$ diffusion of fly ash and blended cement pastes. *Cement Concrete Res.,* 1986; 16(5); 749-59

[38] Lu S, Landis EN, Keane DT. X-ray microtomographic studies of pore structure and permeability in Portland cement concrete *Mater. Struct*., 2006; 39(6); 611-20

[39] Schwan HP, Ferris CD. Four-electrode null techniques for impedance measurement with high resolution *Rev. Sci. Instrum.*, 1968; 39(4); 481–5

[40] Ishai PB, Talary MS, Caduff A, Levy E, Feldman Y. Electrode polarization in dielectric measurements: a review *Meas. Sci. Technol.,* 2013; 24(10); 102001; 21pp

[41] Hsieh G, Ford SJ, Mason TO, Pederson LR. Experimental limitations in impedance spectroscopy: Part VI. Four-point measurements of solid materials systems *Solid State Ionics* 1997; 100; 297-311

Captions for Figures

Fig. 1 (a) Schematic of testing arrangement for 2-point a.c. end-to-end measurements; and (b) laboratory set-up

Fig. 2 (a) Schematic of testing arrangement for 4-point measurements; and (b) laboratory set-up

Fig. 3 (a) Showing the influence of the constant phase element (CPE) on the Nyquist plot – the solid line is the Nyquist plot for a pure capacitor (C=10^{-10}F) in parallel with a resistor (R=1.0 kΩ) and the dashed line is a CPE (C_o=10^{-10} $Fs^{-0.2}$ and p=0.8) in parallel with a resistor (R=1.0kΩ); (b) schematic diagram of Nyquist plot for a saturated porous material showing arc depression angle, α, phase angle, θ^{o}, and impedance, $Z^{*}(\omega)$.

Fig. 4 Nyquist plot for synthetic sponges placed between the electrodes. Saturating liquids indicated.

Fig. 5 (a) Nyquist and (b) Bode plots for PC concrete mixes (error bars are presented on Bode plot and represent ±one standard deviation).

Fig. 6 (a) Nyquist and (b) Bode plots for GGBS concrete mixes (error bars are presented on Bode plot and represent ±one standard deviation).

Fig. 7 (a) Nyquist and (b) Bode plots for FA concrete mixes (error bars are presented on Bode plot and represent ±one standard deviation).

Fig. 8 Proposed circuit model for electrode-sponge-specimen testing configuration.

Fig. 9 Measured and simulated responses for (a) PC concrete (w/b = 0.65) and (b) GGBS concrete (w/b = 0.35). The simulated response is based on the model presented in Fig. 8(a) and circuit parameters in Table 5.

Fig. 10 Influence of sponge saturation liquid on (a) Nyquist and (b) Bode plots for PC concrete (w/b = 0.65).

Fig. 11 Influence of sponge saturation liquid on (a) Nyquist and (b) Bode plots for GGBS concrete (w/b = 0.65).

Fig. 12 Influence of sponge saturation liquid on (a) Nyquist and (b) Bode plots for FA concrete (w/b = 0.65).

Fig. 13 Bode plots obtained using the 4-point testing arrangement presented in Fig. 2 for (a) PC concrete (w/b = 0.65) and (b) GGBS concrete (w/b = 0.35).

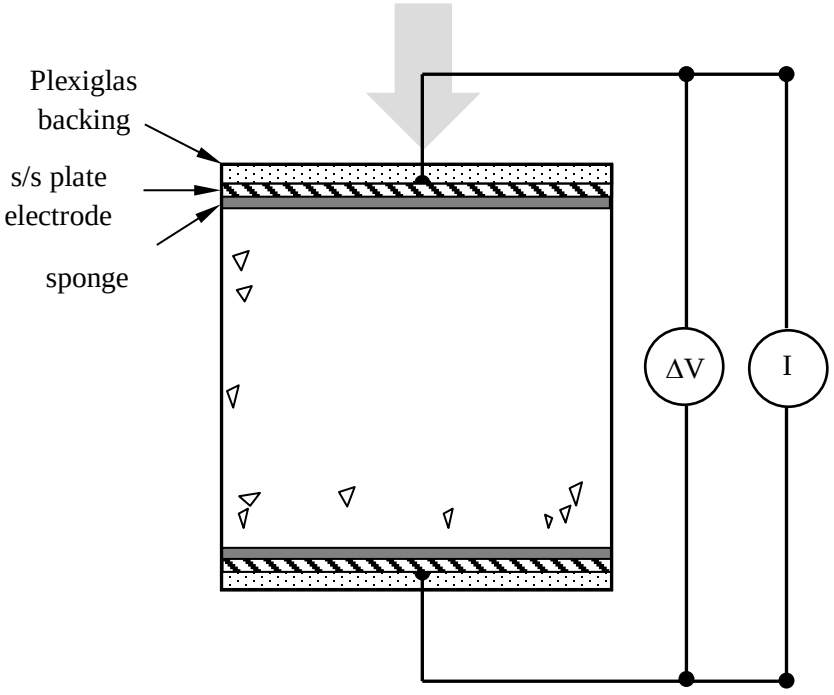

Fig. 1(a)

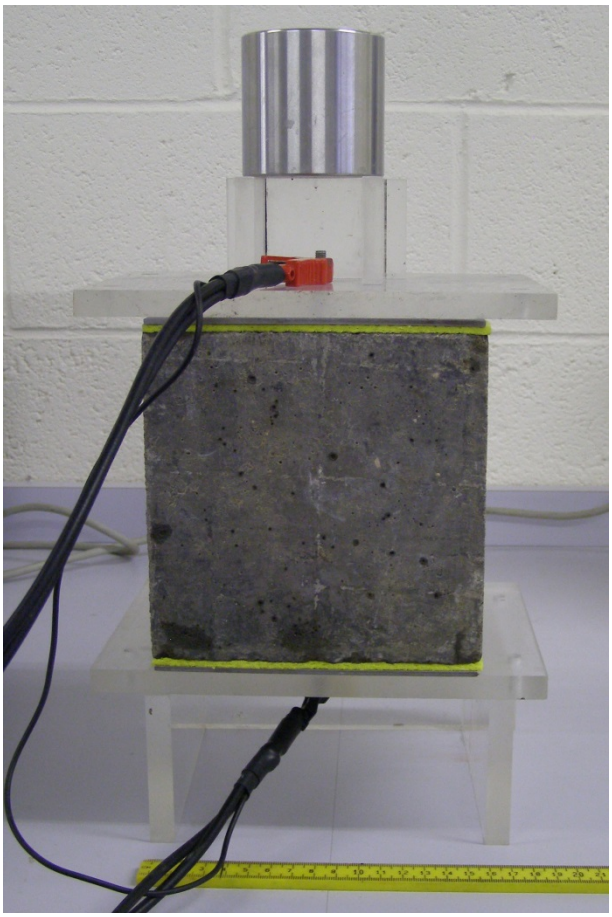

Fig. 1(b)

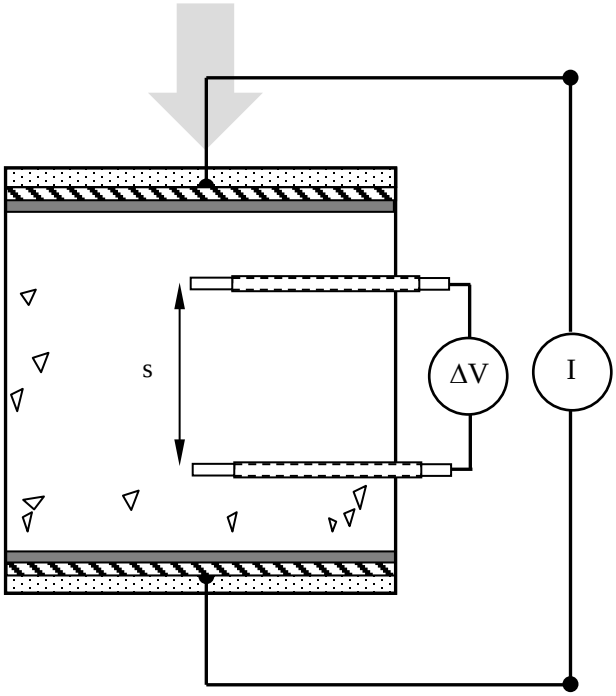

Fig. 2(a)

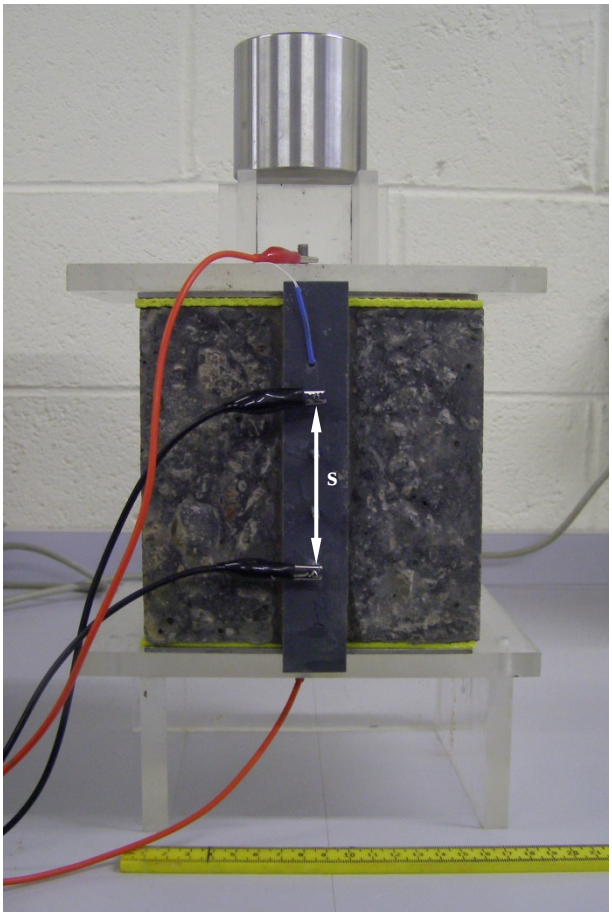

Fig. 2(b)

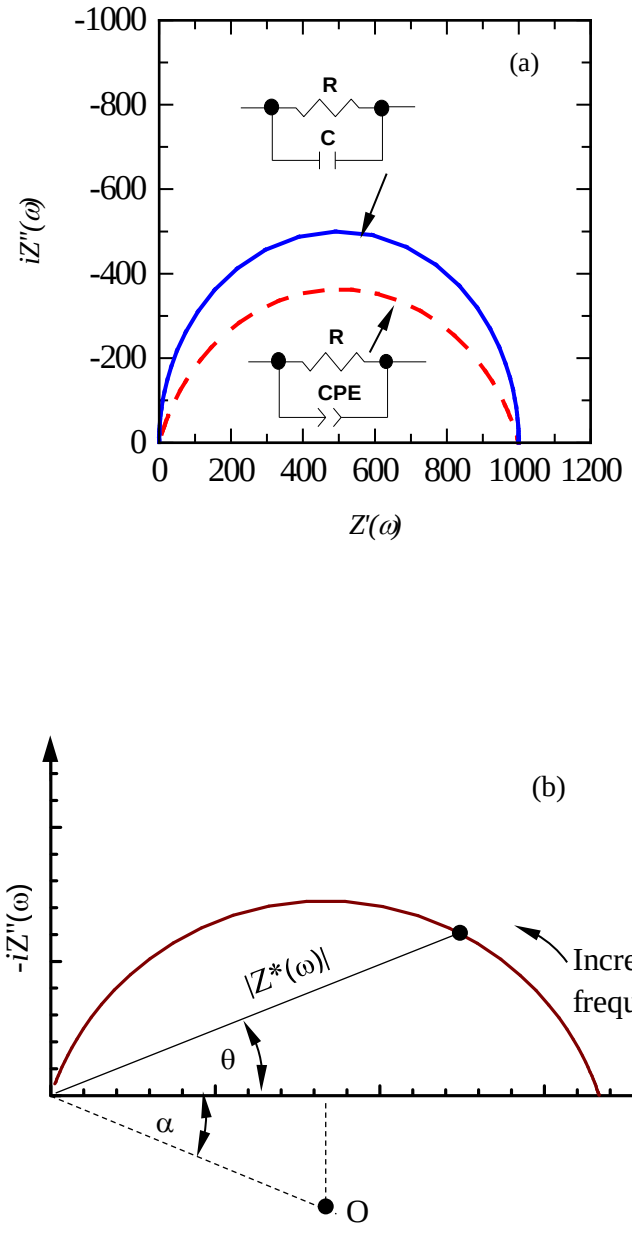
(a)
R
C
R
CPE
-1000
-800
-600
-400
-200
0
0
200
400
600
800
1000
1200
iZ''(ω)
Z'(ω)
(b)
-iZ''(ω)
|Z*(ω)|
θ
α
Increasing
frequency
Z'(ω)
O

Fig. 3

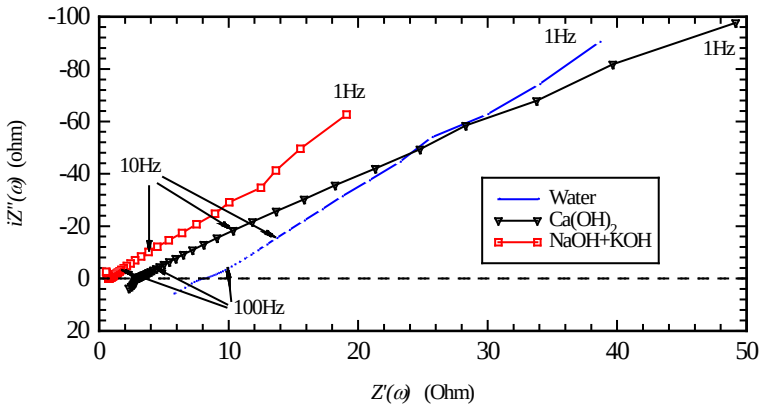
-100
-80
-60
-40
-20
0
20
0
10
20
30
40
50
iZ''(ω) (ohm)
Z'(ω) (Ohm)
1Hz
1Hz
1Hz
10Hz
100Hz
Water
Ca(OH)2
NaOH+KOH

Fig. 4

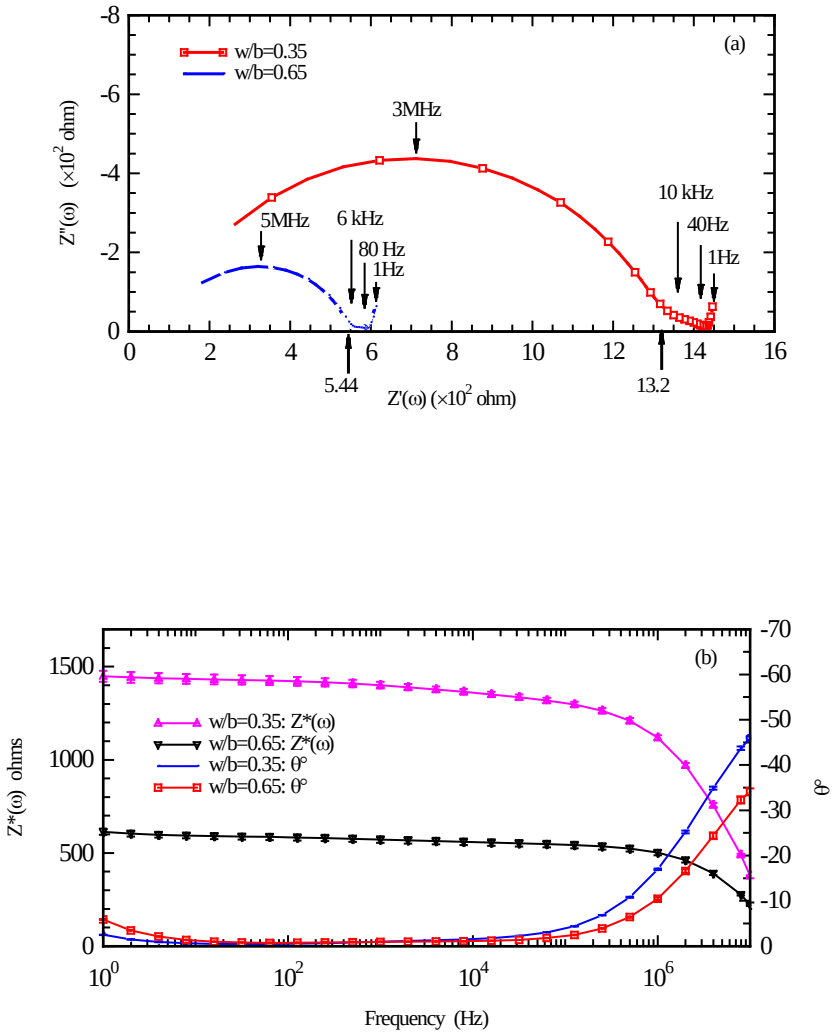
(a)
w/b=0.35
w/b=0.65
3MHz
5MHz
6 kHz
80 Hz
1Hz
10 kHz
40Hz
1Hz
5.44
13.2
Z''(ω) (×10^2 ohm)
Z'(ω) (×10^2 ohm)
(b)
w/b=0.35: Z*(ω)
w/b=0.65: Z*(ω)
w/b=0.35: θ°
w/b=0.65: θ°
Z*(ω) ohms
θ°
Frequency (Hz)

Fig. 5

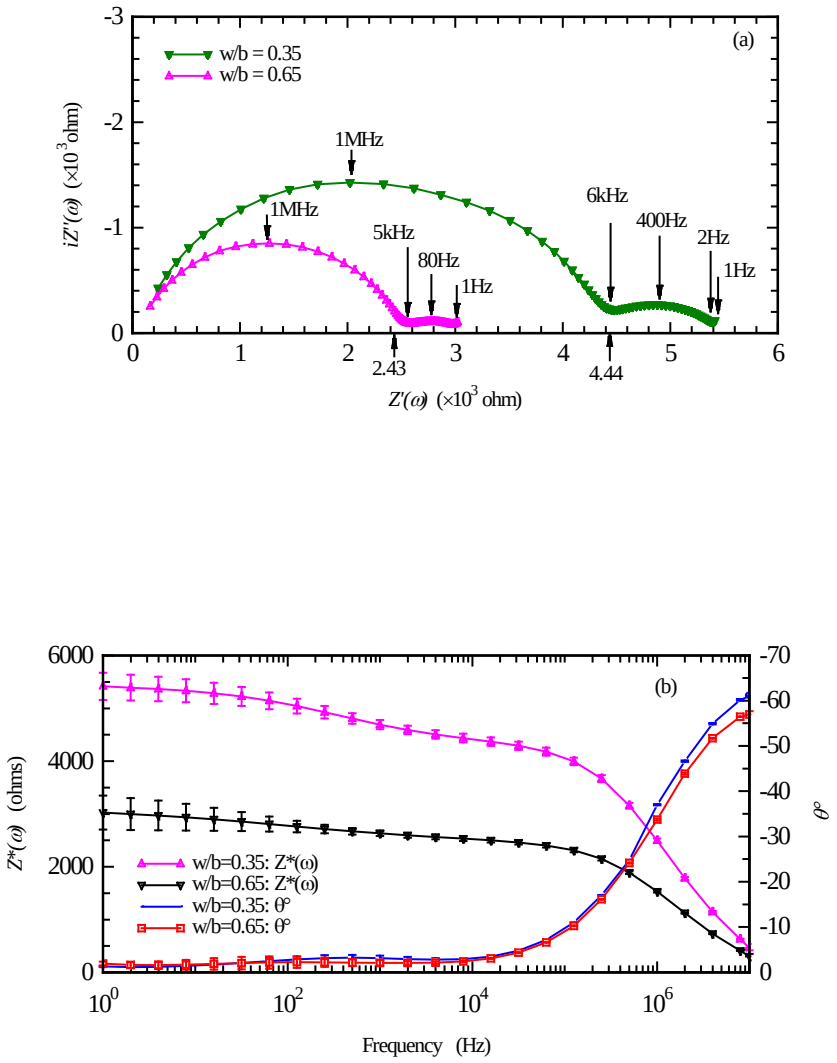
(a)
w/b = 0.35
w/b = 0.65
1MHz
1MHz
5kHz
80Hz
1Hz
6kHz
400Hz
2Hz
1Hz
2.43
4.44
iZ''(ω) (×10^3 ohm)
Z'(ω) (×10^3 ohm)
(b)
w/b=0.35: Z*(ω)
w/b=0.65: Z*(ω)
w/b=0.35: θ°
w/b=0.65: θ°
Z*(ω) (ohms)
θ°
Frequency (Hz)

Fig. 6

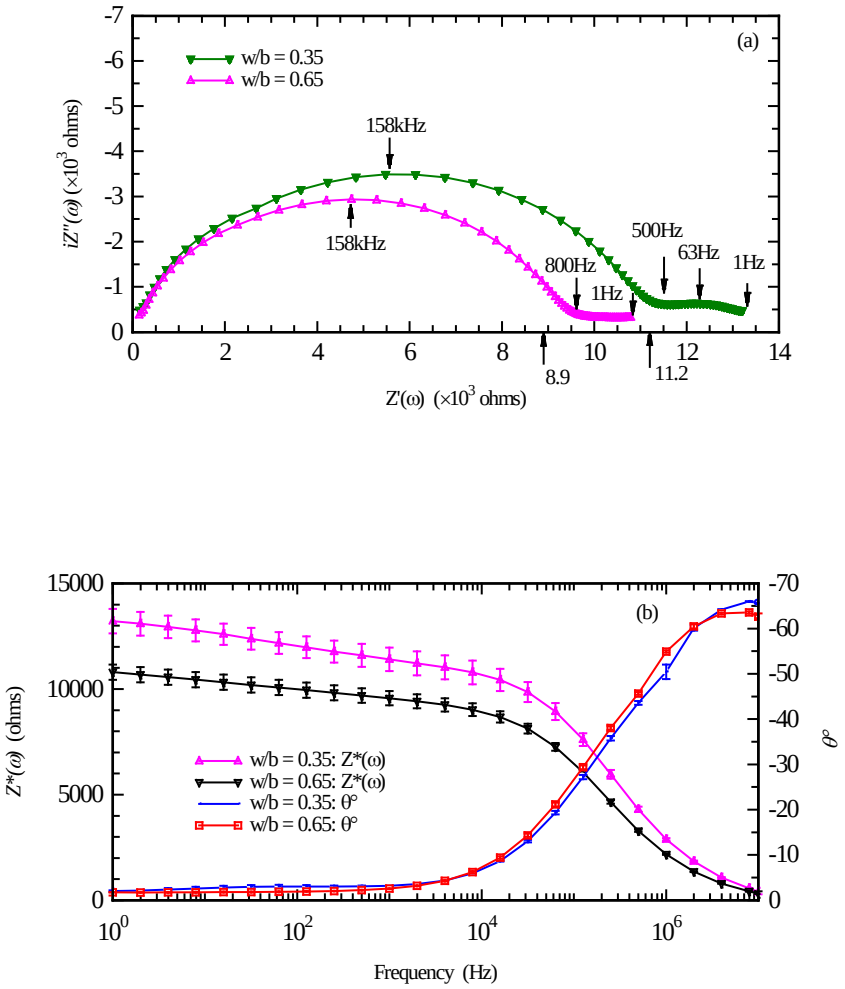
(a)
w/b = 0.35
w/b = 0.65
158kHz
158kHz
500Hz
63Hz
1Hz
800Hz
1Hz
8.9
11.2
iZ''(ω) (×10^3 ohms)
Z'(ω) (×10^3 ohms)
(b)
w/b = 0.35: Z*(ω)
w/b = 0.65: Z*(ω)
w/b = 0.35: θ°
w/b = 0.65: θ°
Z*(ω) (ohms)
θ°
Frequency (Hz)

Fig. 7

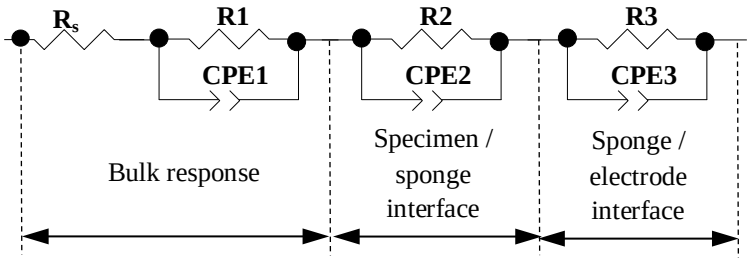
R_s
R1
R2
R3
CPE1
CPE2
CPE3
Bulk response
Specimen / sponge interface
Sponge / electrode interface

Fig. 8

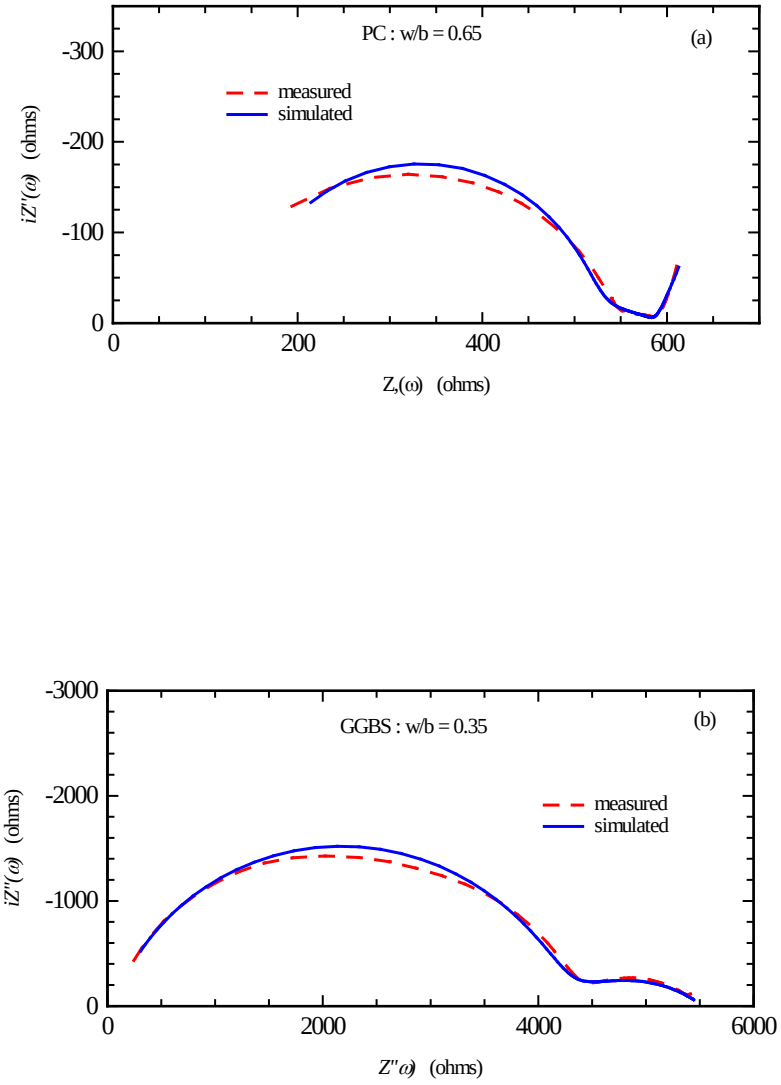
PC : w/b = 0.65
(a)
measured
simulated
-300
-200
-100
0
0
200
400
600
iZ''(ω) (ohms)
Z,(ω) (ohms)
GGBS : w/b = 0.35
(b)
measured
simulated
-3000
-2000
-1000
0
0
2000
4000
6000
iZ''(ω) (ohms)
Z''ω) (ohms)

Fig. 9

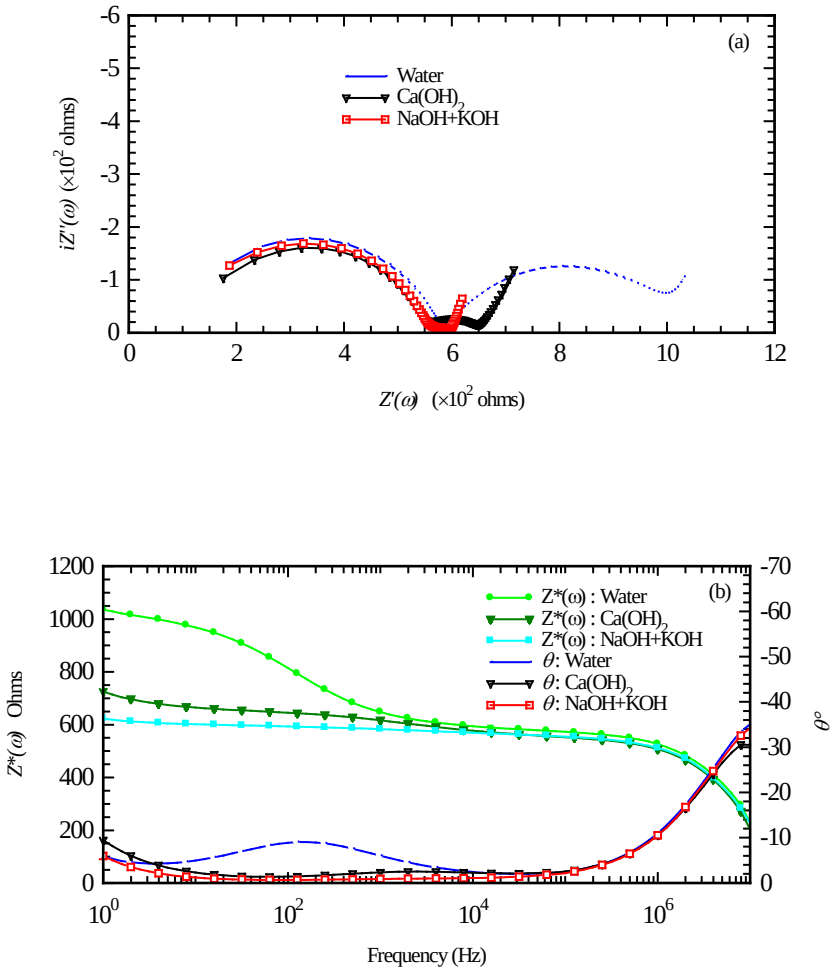
(a)
Water
Ca(OH)2
NaOH+KOH
iZ''(ω) (×10^2 ohms)
Z'(ω) (×10^2 ohms)
(b)
Z*(ω) : Water
Z*(ω) : Ca(OH)2
Z*(ω) : NaOH+KOH
θ: Water
θ: Ca(OH)2
θ: NaOH+KOH
Z*(ω) Ohms
θ°
Frequency (Hz)

Fig. 10

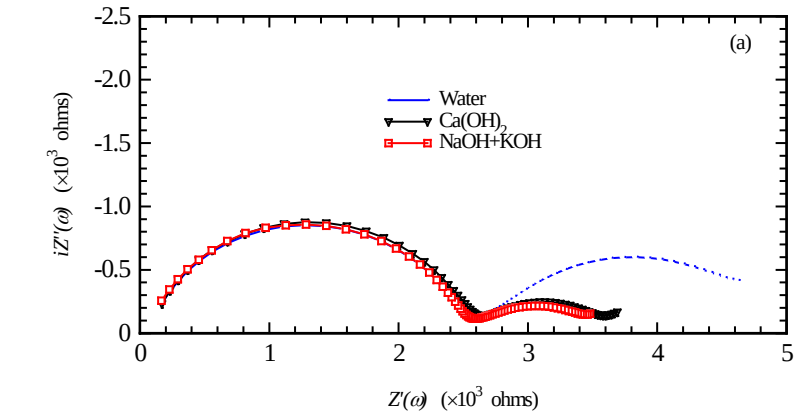
(a)
Water
Ca(OH)2
NaOH+KOH
iZ''(ω) (×10^3 ohms)
Z'(ω) (×10^3 ohms)

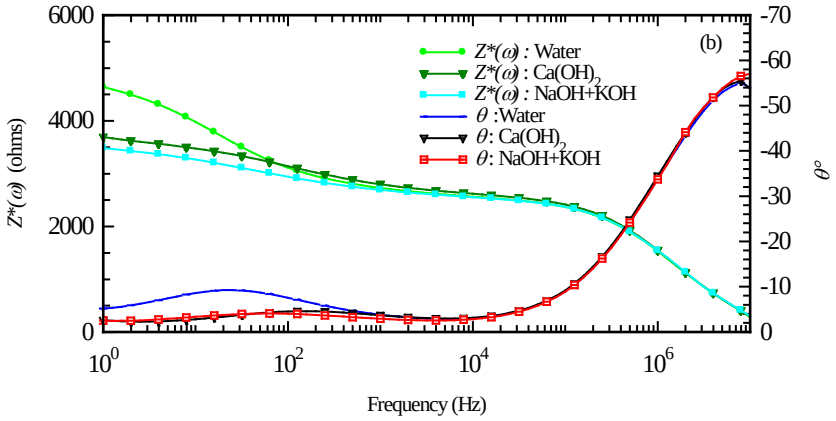
(b)
Z*(ω) : Water
Z*(ω) : Ca(OH)2
Z*(ω) : NaOH+KOH
θ :Water
θ: Ca(OH)2
θ: NaOH+KOH
Z*(ω) (ohms)
θ°
Frequency (Hz)

Fig. 11

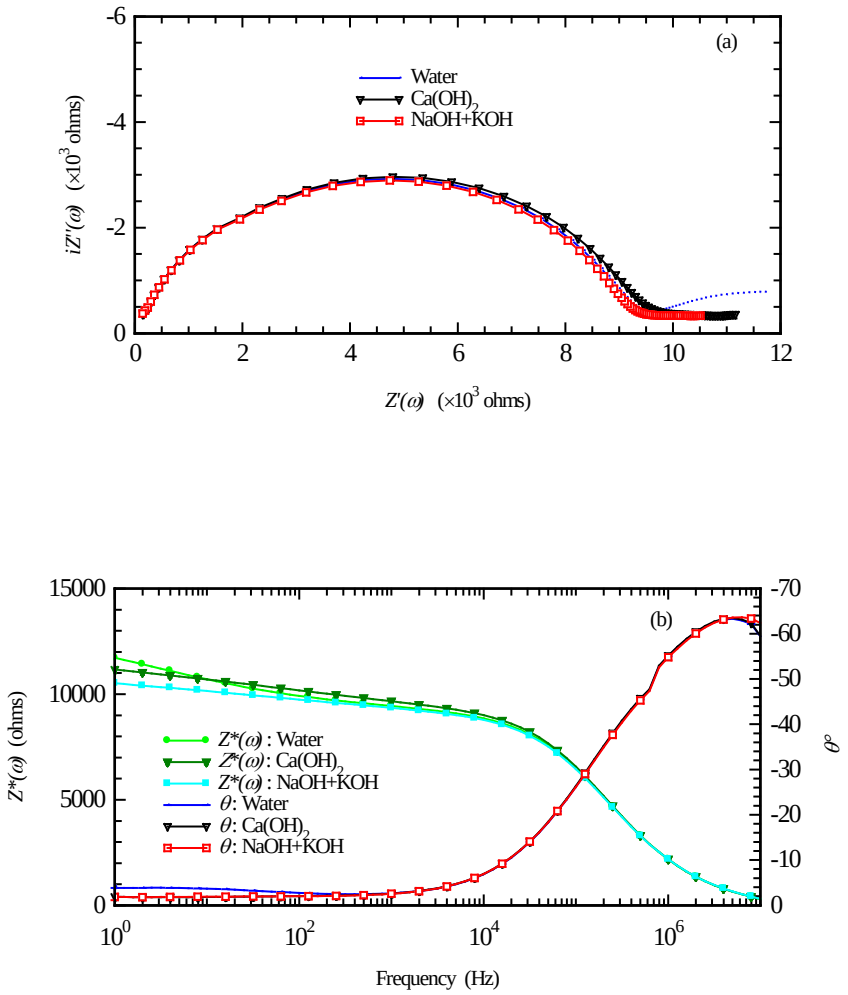
(a)
Water
Ca(OH)2
NaOH+KOH
iZ''(ω) (×10^3 ohms)
Z'(ω) (×10^3 ohms)
-6
-4
-2
0
0
2
4
6
8
10
12
(b)
Z*(ω) : Water
Z*(ω) : Ca(OH)2
Z*(ω) : NaOH+KOH
θ: Water
θ: Ca(OH)2
θ: NaOH+KOH
Z*(ω) (ohms)
θ°
Frequency (Hz)
15000
10000
5000
0
-70
-60
-50
-40
-30
-20
-10
0
10^0
10^2
10^4
10^6

Fig. 12

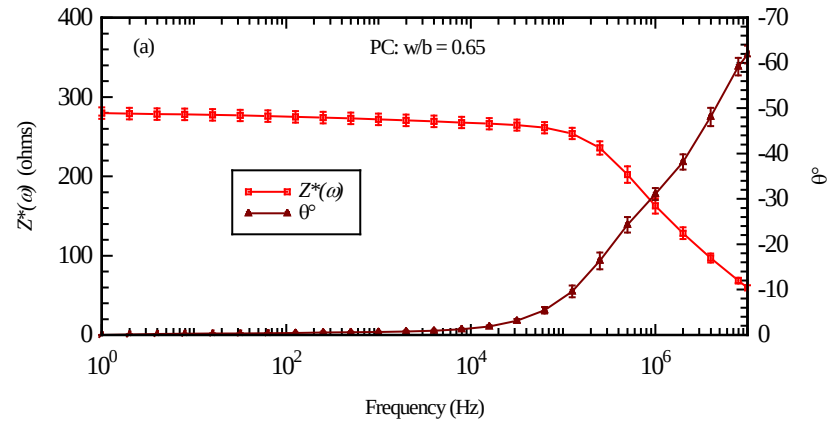
(a)
PC: w/b = 0.65
Z*(ω) (ohms)
θ°
Z*(ω)
θ°
Frequency (Hz)

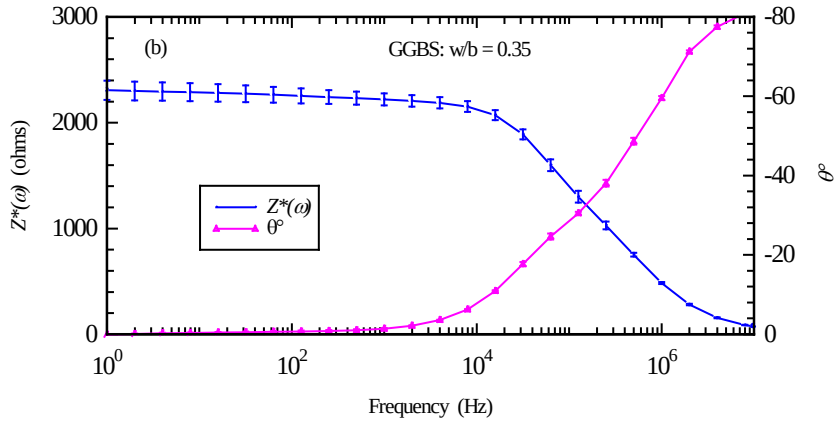
(b)
GGBS: w/b = 0.35
Z*(ω) (ohms)
θ°
Z*(ω)
θ°
Frequency (Hz)

Fig. 13